RSC Advances

PAPER

View Article Online
View Journal | View Issue

Cite this: *RSC Adv.*, 2024, **14**, 8100

Facile synthesis of a rod-like Ni/TiO_2/C nanocomposite for enhanced electromagnetic wave absorption

Yu Hua, Xiaomeng Zhang,* Fulin Chen, Yuantao Sun, Xinyu Wang, Ziliang Wen, Qinghao Tan, Chenxi Sun and Buhe Bateer *

Received 20th December 2023
Accepted 26th February 2024

DOI: 10.1039/d3ra08689e

rsc.li/rsc-advances

In this study, we utilized a simple calcination method to prepare a Ni/TiO_2/C composite, which was synchronously grown from magnetic, semiconductor, and conductive materials. XRD, SEM, Raman, and XPS characterization methods were used to analyze the crystal structure, graphitization degree, morphology size, and valence state of Ni/TiO_2/C, and its electromagnetic wave absorption performance was tested. It was revealed that rod-like Ni/TiO_2/C had good electromagnetic wave absorption performance at a thickness of 1–5.5 mm; in particular, its reflectance reached −40 dB at 3.5 mm and its absorption bandwidth (reflectivity < −10 dB) reached 4.4 GHz (6.0–10.4 GHz) at a thickness of 4.0 mm. It was thus revealed that its electromagnetic wave absorption rate and absorption bandwidth can be regulated by its thickness. Compared with Ni/TiO_2, it was proven that the conductive materials (carbon), magnetic materials (Ni), and semiconductor materials (TiO_2) in the rod-like Ni/TiO_2/C composite can synergistically absorb electromagnetic wave energy through dielectric and magnetic losses.

1. Introduction

With the advent of artificial intelligence, the usage scale and radio-frequency power of large electronic equipment, such as radio signal base stations, television transmitting equipment, navigation transmitting facilities, and MALL devices such as wireless routers, mobile phones, and computers, have increased exponentially.[1–3] Concurrently, electromagnetic radiation in people's living environment has significantly increased, and electromagnetic radiation has become a new form of pollution. It has been proven that long-term, excessive electromagnetic radiation can have many adverse effects on the growth of plants and animals.[4–6] For example, electromagnetic waves can harm the human reproductive system, nervous system, immune system, and can also affect the development of children. In addition, in modern warfare, communication, navigation, fire control, and other systems heavily rely on electromagnetic waves as their main medium and carrier. Therefore, the effective use of electromagnetic waves is one of the key factors that dominate modern warfare.[7–9] Electromagnetic wave absorbing materials are of great significance for human protection and for improving the survivability and anti-strike capability of weapon systems.[10] Developing new electromagnetic wave absorption materials with a thin thickness, light weight, wide frequency band, and multiple functions to meet the development needs of electromagnetic wave pollution protection and military has become an important issue of increasing concern.[11]

The current research on electromagnetic wave absorbing materials mainly focuses on carbon materials,[12] metal oxides,[13] conductive polymers,[14] composite materials, *etc.*[15] Metal oxides were one of the earliest materials used to absorb electromagnetic waves. By studying the electromagnetic wave absorption properties of Fe_3O_4,[16] ZnO,[17] MnO_2,[18] SnO_2,[19] TiO_2,[20] and other oxides, it was found that the above substances have the advantages of simple preparation, low cost, high stability, and high electromagnetic wave absorption value. TiO_2 is an N-type semiconductor; therefore, when an electromagnetic wave with an energy greater than the bandgap width (E_g) is injected into TiO_2, the electrons in the valence band are excited and jump to the conduction band, thereby consuming the energy of the electromagnetic wave. Therefore, TiO_2 can be used as an electromagnetic wave absorbing material.[21] In order to make TiO_2 more widely used in the field of electromagnetic wave absorption, scientists began to study the electromagnetic wave absorption performance of TiO_2 composites. While TiO_2 as a semiconductor can improve the impedance mismatching of the carbon and Ni phases, Sun *et al.*[22] solved the problem of the low X-band absorptivity by enhancing the magnetic loss capability after combining Ni with TiO_2. Wan *et al.*[23] prepared a TiO_2/C composite to improve the electrical loss ability through the interface polarization of TiO_2 and C materials, thus achieving a strong absorption in the C band. Electromagnetic wave absorbing materials consume electromagnetic wave energy through electrical loss and magnetic loss; however, TiO_2 can

College of Materials and Chemical Engineering, Heilongjiang Institute of Technology, Harbin 150050, China. E-mail: zhxm0616@126.com; bate1976@sina.com

only obtain a single loss composite material for absorbing electromagnetic waves after being combined with magnetic loss materials or electrical loss materials, and it cannot achieve the synergistic effect of both electrical and magnetic loss. Zhang *et al.*[24] combined TiO_2 with Fe_3O_4 and carbon fiber, and obtained an electromagnetic wave absorbing material with an absorption bandwidth of 5.65 GHz (RL < −10 dB) through the synergistic effect of electrical loss and magnetic loss. From the above research, we know that TiO_2 is a traditional electromagnetic wave absorbing material. Loading nanometals onto TiO_2 to form a composite material can improve the surface resistance of TiO_2. In particular, when combined with magnetic materials and carbon materials at the same time, the electromagnetic wave absorption effect is more obvious.[25] However, there is scant research on the electromagnetic wave properties of synchronous generation TiO_2, electric, and magnetic ternary composite materials.

In this paper, Ni/TiO_2/C composite was prepared by a simple calcination method, and its structural properties were characterized by SEM, XRD, and XPS. The electromagnetic wave absorption performance was analyzed by a vector network analyzer, and it was found that the reflectivity value of Ni/TiO_2/C at 3.5 mm was −40 dB. Compared with Ni/TiO_2, it was found that the electromagnetic wave absorption performance of Ni/TiO_2/C was significantly improved, which proved that electromagnetic synergy effect could allow obtaining superior electromagnetic wave absorption materials.

2. Experimental section

2.1. Materials

Nickel acetate tetrahydrate ($Ni(CH_3COO)_2 \cdot 4H_2O$), ethylene glycol ($(CH_2OH)_2$), tetrabutyl titanate ($Ti(OC_4H_9O)_4$), anhydrous ethanol, and citric acid ($C_6H_8O_7$) were obtained as analytically pure chemicals from Aladdin Reagent Co., Ltd.

2.2. Experimental methods

Ni/TiO_2/C composite was prepared by a calcination method. The typical process was as follows: 0.01 mol of $Ni(CH_3COO)_2 \cdot 4H_2O$ was added to 60 mL ethylene glycol and stirred magnetically at room temperature for 30 min until $Ni(CH_3COO)_2 \cdot 4H_2O$ was completely dissolved. Next, 0.01 mol $Ti(OC_4H_9O)_4$ was added to the above mixed solution, and the solution was stirred at room temperature until a light-blue precipitate was produced. The precipitate was centrifuged with anhydrous ethanol 5 times to remove any impurities. The centrifuge speed was 4500 RPM for 5 min each time. The cleaned precipitates were dried at 60 °C for 4 h to obtain a blue powder. Then the precursor was mixed with citric acid powder according to the mass ratio of 1 : 1 and put into a porcelain boat. Under a nitrogen atmosphere (50 mL min^{-1}), the temperature was raised to 600 °C at 5 °C min^{-1} and kept there for 2 h, until the Ni/TiO_2/C composite was finally obtained. The comparison sample Ni/TiO_2 was prepared by the above method without mixing with citric acid powder. The preparation process is shown in Fig. 1.

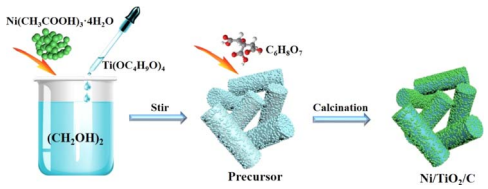

Fig. 1 Illustration of the synthesis of Ni/TiO_2/C.

2.3. Characterization

Scanning electron microscopy (SEM, Hitachi SU5000, Japan) was used to observe the size, microstructure, and morphology of the materials. Energy dispersive spectrometry (EDS, Uitiemmax40, UK) was used to analyze the content and distribution of elements on the surface of the material at an operating voltage of 15 kV. X-Ray diffractometry (XRD, Rigaku D/max-IIIB, Japan) was used to characterize the crystal structure of the material under the test conditions of Cu and K radiation, operating voltage of 40 kV, and current of 40 mA. The Physical Properties Measurement System (PPMS, Quantum Design Inc., USA) was used to measure the magnetic properties at 300 K and a maximum magnetic field of 20 kOe. A differential thermal analyzer (NETZSCH, STA-449F3, Germany) was used to test the C content in the material. A Raman spectrometer (HR800-Horiba Jobin Yvon, France) was used to analyze the degree of graphitization. X-Ray photoelectron spectroscopy (XPS, VG ESCALAB MK II, UK) was performed for assessing the surface chemical composition and valence state of the materials using a dispersive X-ray source. The sample and paraffin wax were mixed at a mass ratio of 3 : 7 and pressed into a coaxial ring with an outer diameter of 7.0 mm, an inner diameter of 3.0 mm and a thickness of 3.0 mm. The electromagnetic wave absorption parameters at 2–18 GHz frequencies were measured at room temperature by a coaxial test method using a vector network analyzer (Anritsu, MS4644B, Japan).

3. Results and discussion

The morphology and structure of Ni/TiO_2/C were characterized by scanning electron microscopy (SEM). It could be seen from Fig. 2a–d that Ni/TiO_2/C had a rod-like structure with a diameter between 500 nm to 1 μm and a length less than 10 μm. The

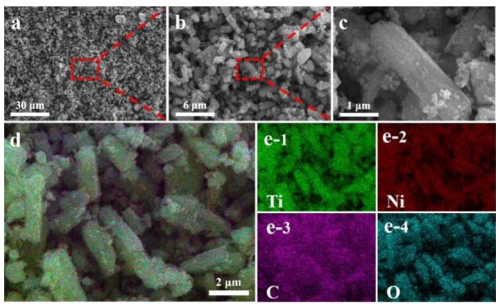

Fig. 2 Scanning electron microscopy (SEM) images of Ni/TiO_2/C (a–d) and (e) EDS maps.

carbon material was distributed in the TiO_2 rod-like structure, and spherical monodisperse Ni particles firmly wrapped and adhered to the surface of the micron rod. In the preparation process, Ni^{2+} ions were adsorbed in solution and then reduced to Ni nanoparticles by calcination. A uniform loading of Ni nanoparticles was beneficial to improve the electromagnetic wave absorption performance of the Ni/TiO_2/C composite through magnetic loss. Fig. 2e presents the further analysis of the elemental composition of Ni/TiO_2/C using the corresponding energy dispersive X-ray spectroscopy (EDS). Fig. 2d shows the overlap of the individual EDS maps in Fig. 2e. It can be seen from Fig. 2e that there were C, Ti and Ni, and O elements in the Ni/TiO_2/C composite material, and that the distribution of C, Ti and Ni, and O elements was uniform, which also proved that Ni/TiO_2/C was a uniform composite material.

X-Ray Diffraction (XRD) technology can be used to analyze the structural composition of a samples[26] Fig. 3a shows the XRD analysis patterns of the prepared Ni/TiO_2/C and Ni/TiO_2 samples. From Fig. 3a, we can see that Ni/TiO_2/C displayed strong diffraction peaks at $2\theta = 44.492°$, 51.846°, and 76.376°, which corresponded to the [111], [200], and [220] crystal faces of Ni, respectively. These were consistent with the standard PDF card 65-2868 of Ni. The [111], [200], and [220] crystal faces were the most representative ones for the FCC structure, which was consistent with the characterization results for Ni, proving that the prepared sample Ni/TiO_2/C contained a face-centered cubic lattice structure with Ni. The diffraction peaks at $2\theta = 25.303°$, 53.884°, and 55.059° corresponded to the [101], [105], and [211] crystal faces of TiO_2, respectively. These were consistent with the standard PDF card 65-5714 of TiO_2, where the [101] and [105] surfaces belonged to the {100} surface family, and the atoms on the {100} surface were highly isotropic, because they were equivalent in their position in the crystal surface. This means that the spacing of the atoms on the {100} crystal surface was larger than that on the other crystal surface, and the arrangement was more uniform and more stable, which makes them better able to reflect the characteristics of the tetragonal crystal system. Also, [211] belonged to the crystal surface family {210}, which is also a characteristic crystal surface of the tetragonal crystal system. The occurrence of {100} and {210} crystal surfaces in the XRD analysis showed that TiO_2 with a tetragonal crystal system structure had been successfully prepared. The diffraction peak at $2\theta = 26.542°$ corresponded to the [002] crystal face of C, which also corresponded to the standard PDF card 65-6212 of C. The above characterization indicates that Ni/TiO_2/C was a composite material composed of Ni, TiO_2, and C. The diffraction peaks of the Ni/TiO_2 sample included the standard peaks of Ni and TiO_2, which could indicate that the sample was composed of Ni and TiO_2. XRD characterization thus proved that the Ni/TiO_2/C and Ni/TiO_2 composites were successfully prepared.

The approximate size of the particles can be calculated by Scherrer's formula.[27]

$$D = \frac{K\gamma}{B\cos\theta} \quad (1)$$

where, K is Scherrer's constant. If B represents the full width at half maximum of the diffraction peak, then $K = 0.89$. If B represents the integrated width of the diffraction peak, then $K = 1$. D is the average thickness (in Å) of the grains perpendicular to the crystal plane direction. B is the measured diffraction peak width, which needs to be converted to radians (rad) during the calculation. θ is the Bragg diffraction angle, measured in degrees. γ is the X-ray wavelength, which is typically 1.54056 Å for Cu Kα.

In the Ni/TiO_2/C system, the full width at half maximum (FWHM) of Ni was 0.348, 0.346, and 0.327, respectively, and the maximum FWHM was thus 0.348. By adopting the Scherrer constant (K) of 0.89 and utilizing the maximum FWHM, the particle diameter of Ni within the Ni/TiO_2/C system was calculated to be 24.1 nm. Similarly, in the Ni/TiO_2 system, the FWHM of Ni was 0.441, 0.333, and 0.455, respectively, and the maximum FWHM was thus 0.455. This allows the calculation of the particle diameter of Ni in the Ni/TiO_2 system as 22.8 nm. In Fig. 3a, the diffraction peak of the [111] crystal plane of Ni in Ni/TiO_2/C was narrower and higher than that in Ni/TiO_2, which was consistent with the calculated results. The reason for the larger Ni particles in Ni/TiO_2/C was that the C material could adsorb Ni atoms, thus controlling the formation of its crystal nuclei and crystal growth.[28] The XRD patterns of the Ni/TiO_2/C and Ni/TiO_2 samples did not show obvious miscellaneous peaks, indicating that no other substances were formed during the preparation process. The strong magnetic material Ni, semiconductor material TiO_2, and conductor C in the Ni/TiO_2/C composite could achieve a better electromagnetic wave energy loss effect through their respective electromagnetic wave absorption performances and the interface polarization of the three materials.

The prepared Ni/TiO_2/C and Ni/TiO_2 samples exhibited magnetism because they contained the ferromagnetic Ni, and their magnetic properties could thus be tested by a vibrating sample magnetometer. Fig. 3b shows the hysteresis loops of the Ni/TiO_2/C and Ni/TiO_2 samples tested at a temperature of 300 K and a maximum magnetic field intensity of 20 kOe. When the magnetic field intensity was increased to 5000 Oe, the magnetization of the two samples changed greatly, with the values reaching 10 and 16 emu g^{-1}, respectively. When the magnetic

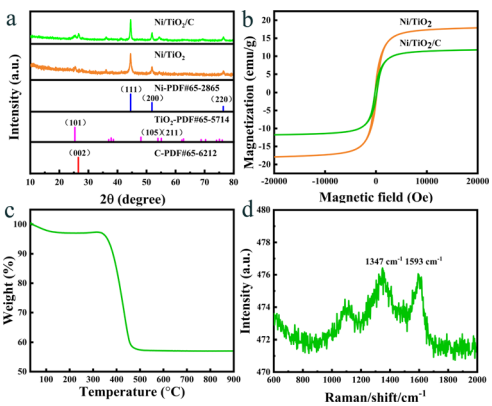

Fig. 3 (a) XRD patterns and (b) hysteresis loops of Ni/TiO_2/C and Ni/TiO_2, (c) TGA pattern and (d) Raman spectra of Ni/TiO_2/C.

field intensity was increased from 5000 Oe to 20 kOe, the specific saturation magnetization of the two samples did not increase much, but tended toward a saturation state. It could be seen from the Fig. 3b that the specific saturation magnetization values of Ni/TiO_2/C and Ni/TiO_2 were 12 and 18 emu g^{-1}, respectively. The remanence values were 1.70 and 2.58 emu g^{-1}, respectively. The coercivity values were all 193 Oe. The specific saturation magnetization of Ni/TiO_2/C was 6 emu g^{-1} lower than that of Ni/TiO_2, which was caused by the fact that the loading of C in Ni/TiO_2/C increased the non-magnetic substances content. The magnetic source of the two samples was from ferromagnetic Ni, where the Ni particles in the two samples could improve the electromagnetic wave absorption performance through magnetic loss. In Ni/TiO_2/C and Ni/TiO_2, the remanence and coercivity values were similar, with a slight difference, which may be caused by the different particle sizes and contents of Ni.

The content of C in Ni/TiO_2/C was analyzed by thermogravimetric analysis (TGA). Fig. 3c shows the thermogravimetric curves of Ni/TiO_2/C at 30–1000 °C, at a heating rate of 10 K min^{-1}, and air flow rate of 50 mL min^{-1}. As can be seen from Fig. 3c, Ni/TiO_2/C had a quality loss of 3% in the temperature range of 30–150 °C, which may have been caused by residues of low-transformative substances (water, ethanol, *etc.*) in the cleaning process.[29] In the range of 240–310 °C, the sample mass increased slightly due to the oxidation of Ni nanoparticles, resulting in a small increase in the curve. As the temperature continued to rise, C combustion caused the sample quality to decline rapidly until the temperature increased to 500 °C. It is generally believed that the process of oxidation of Ni nanoparticles into the final product NiO will partially compensate the mass loss caused by C combustion. Therefore, the C content was estimated according to the following formula:[30]

$$C\ wt\% = (1 - wt\% - wt\%_{organics})M(NiO)/M(Ni) \quad (2)$$

where wt% is the mass percentage content, and M is the molecular weight of Ni and NiO. The relative content of C in Ni/TiO_2/C as calculated by the above formula was about 43.3%, which was close to the EDS analysis result.

The graphitization degree of carbon materials in the Ni/TiO_2/C composite was analyzed by Raman tests. As shown in Fig. 3d, two distinct characteristic peaks could be observed at 1347 and 1593 cm^{-1}, corresponding to the D-band and G-band, respectively, and the intensity ratio was close to 1. This proved that the formed carbon had disordered defects, which may be due to the low preparation temperature and the doping of Ni and TiO_2 materials. The composite of defective carbon with Ni and TiO_2 is conducive to the consumption of incoming electromagnetic wave energy and the absorption of electromagnetic waves.

X-Ray photoelectron spectroscopy (XPS) is a method for the in-depth study of the valence states of the components of materials.[31] The prepared Ni/TiO_2/C composite was analyzed by XPS. The XPS diagrams are shown in Fig. 4, showing that the prepared Ni/TiO_2/C composite was composed of four elements: Ni, Ti, O, and C. The atomic concentrations of Ni, Ti, O, C in the Ni/TiO_2/C composite were 0.79%, 2.53%, 18.94%, and 77.74%,

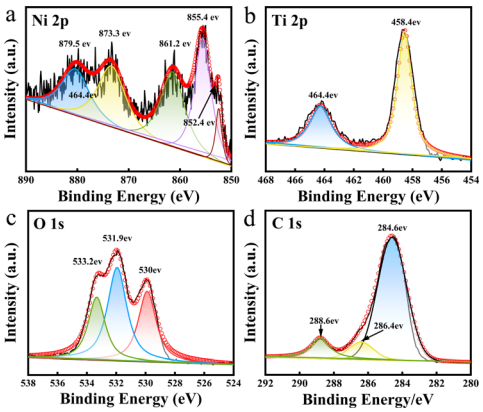

Fig. 4 XPS spectra in the (a) Ni 2p region; (b) Ti 2p region; (c) O 1s region; and (d) C 1s region for Ni/TiO_2/C.

respectively. Fig. 4a presents the XPS map for Ni 2p, where four peaks could be observed at 855.4, 861.2, 873.3, and 879.5 eV, corresponding to the positions of Ni^{2+} and its satellite peaks. This proved that Ni^{2+} transformed into Ni when calcined in air. The reason for the characteristic peak of the oxidation state of Ni at 852.4 eV was that a trace amount of Ni and O formed NiO during the preparation process. Fig. 4b shows the XPS diagram of Ti 2p, displaying two peaks at 458.4 and 464.4 eV, which were the characteristic peaks of the Ti $2p_{3/2}$ and Ti $2p_{1/2}$ orbits. This proved the existence of Ti^{4+}. Fig. 4c shows the XPS diagram of O 1 s, which displays three peaks located at 530, 531.9, and 533.2 eV, respectively. Fig. 4c proves that O^{2-} existed in the composite material, and arose from TiO_2 and trace Ni oxidation. Fig. 4d shows the XPS diagram of C 1s, where it can be seen that the C 1s spectrogram had three peaks, namely at 284.6, 286.4, and 288.6 eV. Their binding energy was concentrated at 284.6 eV, and was related to the C–C bond. The XPS results further confirmed that the prepared Ni/TiO_2/C composite was composed of Ni, TiO_2, and C.

The electromagnetic wave absorption properties of a material are mainly determined by the electromagnetic parameters, including the complex dielectric constant (ε_r) and the complex permeability (μ_r). Therefore, a coaxial ring was prepared by mixing Ni/TiO_2/C or Ni/TiO_2 with paraffin wax at the specific gravity of 3 : 7, respectively, and the real part (ε') and imaginary part (ε'') of the complex permittivity and the real part (μ') and imaginary part (μ'') of the complex permeability were measured, and then the following formula was used for the specific calculations and analysis.[32,33]

$$\varepsilon_r = \varepsilon' + j\varepsilon'' \quad (3)$$

$$\mu_r = \mu' + j\mu'' \quad (4)$$

$$\tan \delta\varepsilon = \frac{\varepsilon''}{\varepsilon'} \quad (5)$$

$$\tan \delta\mu = \frac{\mu''}{\mu'} \quad (6)$$

$$Z_{in} = \sqrt{\frac{\mu_r}{\varepsilon_r}} \tan h \sqrt{j\frac{2\pi f d\sqrt{\mu_r \varepsilon_r}}{c}} \quad (7)$$

$$RL = 20 \log\left|\frac{Z_{in} - 1}{Z_{in} + 1}\right| \quad (8)$$

where Z_{in} is the electromagnetic wave incident impedance of the material, j is the imaginary unit, f is the electromagnetic wave frequency, d is the thickness of the material, ε_r and μ_r are the complex dielectric constant and complex permeability, respectively, and c is the speed of light in vacuum. Also, RL is the reflectivity of the material, and when the reflection loss rate is lower than −10 dB (RL < −10 dB), it means that more than 90% of the electromagnetic wave can be absorbed. Further, ε' and ε'' represent the energy storage capacity and loss capacity of the material to the electromagnetic field, respectively; and μ' and μ'' represent the storage capacity and loss capacity of the material to the electromagnetic field energy, respectively. In the formula, the ratio of the imaginary part and the real part of the complex dielectric constant is defined as the tangent of the dielectric loss angle (tan $\delta\varepsilon$), and $\delta\varepsilon$ is the dielectric loss angle. Further, the ratio of the real and imaginary parts of the complex permeability is defined as the tangent of the magnetic loss angle (tan $\delta\mu$), where $\delta\mu$ is the magnetic loss angle.

Fig. 5 shows the relationship between the complex permittivity and complex permeability of the sample with the change of frequency. It can be seen from Fig. 5a that the ε' of Ni/TiO_2/C in the 2–18 GHz band generally showed a downward trend, with the value decreasing from 9.54 to 5.43. It dropped slowly in the 2–6 GHz band, then rapidly in the 6–8 GHz band, before dropping to 5.47 near 10 GHz, and then slowly and slightly rising in the 10–12 GHz band, and then dropped slowly again. The ε' of Ni/TiO_2 remained basically unchanged in the 2–14 GHz band, but fluctuated slightly in the 14–15 GHz band, first increasing, then decreasing to the minimum value of 4.46, and then slowly increasing to 5.10 in the 15–18 GHz band.

In Fig. 5b, in the 2–18 GHz frequency band, the value of ε'' of Ni/TiO_2/C increased slowly from 3.34, and reached a maximum value of 5.17 in the 7–8 GHz frequency band. Then the value of ε'' of Ni/TiO_2/C decreased, and the curve formed a large wide peak in the 6–10 GHz frequency band. The minimum value was 2.54 in the range of 13–14 GHz. There was a small fluctuation in the 14–18 GHz frequency band. The ε'' of Ni/TiO_2 generally remained above 0 in the 2–14 GHz frequency band and decreased from 0.65 to a minimum value of 0.03 in the 2–14 GHz band. There was a small peak in the 14–15 GHz frequency band, where the peak value was 0.25. The ε'' then increased slowly to 0.45 in the 15–18 GHz band.

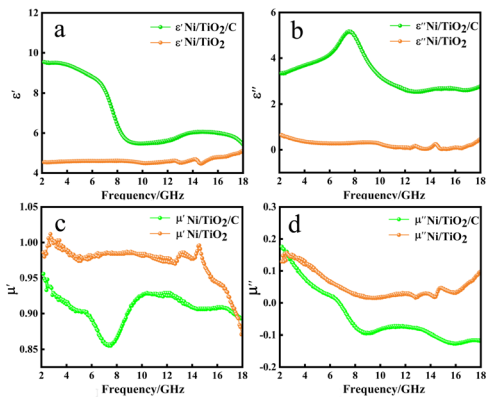

Fig. 5 Complex permittivity and permeability of Ni/TiO_2/C, Ni/TiO_2 and paraffin composites, (a) real parts of the permittivity; (b) imaginary parts of the permittivity; (c) real parts of the permeability; (d) imaginary parts of the permeability.

In Fig. 5c, the μ' of Ni/TiO_2/C decreased in the 2–7 GHz frequency band, decreasing from 0.95 to the lowest point 0.86, and then rapidly rose to 9.24 in the 7–10 GHz frequency band, before plateauing in the 10–12 GHz frequency band, where it basically remained unchanged. The μ' of Ni/TiO_2/C decreased in the 12–14 GHz frequency band and remained basically unchanged in the 14–16 GHz band, before declining to 0.89 in the 16–18 GHz band. The μ' of Ni/TiO_2 rose slightly and then decreased at the beginning, whereby the curve formed a small peak in the 2–5 GHz band with an μ' value of Ni/TiO_2 of 1. The curve then rose slowly and then decreased slowly in the 5–13 GHz frequency band and formed two small peaks, with the higher of the two peaks having a peak value of 0.99, but then the μ' of Ni/TiO_2 quickly dropped to 0.87.

In Fig. 5d, the μ'' of Ni/TiO_2/C decreased with the increase in frequency in the 2–9 GHz frequency band, with the μ'' value decreasing from 0.17 to −0.09, then dropping below 0 at 6.8 GHz, and then slowly rose in the frequency band of 9–12 GHz, before slowly decreasing to −0.12 in the frequency band of 12–16 GHz. It slowly rose again in the 16–18 GHz band. The μ'' of Ni/TiO_2 decreased with the increase in frequency in the 2–9 GHz band, with the μ'' value decreasing from 0.14 to the lowest point of 0.02, and then rose slowly to 0.09 in the 9–18 GHz band, among which there was a small fluctuation near 15 GHz. The μ'' value of Ni/TiO_2 was generally maintained above 0. It could be seen from Fig. 5c and d that the complex permeability values of Ni/TiO_2/C and Ni/TiO_2 both showed a decreasing trend with the increase in frequency.

Through the analysis of Fig. 5, we could find that the complex dielectric constant values of Ni/TiO_2/C for ε' and ε'' were higher than the Ni/TiO_2, while the Ni/TiO_2/C complex permeability μ' and μ'' values overall were lower than those of Ni/TiO_2 for μ' and μ''. This is because the composite with carbon materials reduced the specific gravity of magnetic materials in the materials, compared with Ni/TiO_2, resulting in an increase in the complex dielectric constant and a decrease in the complex permeability of Ni/TiO_2/C. The above results indicated that the unique interface between Ni, TiO_2, and C not only produced sufficient lattice defects for inducing dipolar polarization, but also induced an uneven spatial charge distribution for enhancing the interface polarization. Therefore, abundant heterogeneous interfaces of materials can reinforce the aforementioned polarization relaxation process.

In order to further analyze the electrical loss and magnetic loss capacity of the materials, the dielectric loss and magnetic loss values were calculated by using formulae (4) and (5). In Fig. 6a, the electrical loss of Ni/TiO_2/C can be seen to increase

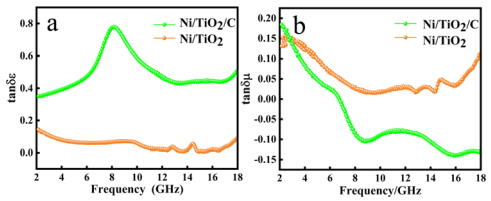

Fig. 6 Complex permittivity and permeability of $Ni/TiO_2/C$, Ni/TiO_2, and the paraffin complex: (a) dielectric loss and (b) magnetic loss.

with the increase in frequency in the 2–9 GHz range, decreases with the increase in frequency in the 9–13 GHz range, and basically remained unchanged in the 13–17 GHz range, before slowly increasing in the 17–18 GHz range. The curve generally showed an upward trend, with the value increasing from the initial value of 0.35 to 0.51, among which there was a large change in the 6–10 GHz range, where the curve presented a broad peak, with a value of up to 0.78 near 9 GHz. However, the electrical loss of Ni/TiO_2 decreased from 0.14 to 0.08 with the increase of frequency in the 2–18 GHz band, with a small fluctuation near 15 GHz, where a small peak was formed, with a minimum value of 0.008.

In Fig. 6b, it could be seen that the magnetic loss of $Ni/TiO_2/C$ decreased rapidly with the increase in frequency in the frequency band at 2–9 GHz. In the frequency band at 9–16 GHz, the magnetic loss rose slowly at first and then dropped slowly to the lowest point, with a minimum value of −0.14, and then the magnetic loss rose slowly again. In the 2–18 GHz range, the overall value decreased from the initial value of 0.18 to −0.13. However, the magnetic loss of Ni/TiO_2 in the range of 2–18 GHz decreased first and then increased with the increase in frequency, with an overall downward trend, where the overall value decreased from 0.14 to 0.11, in which the minimum value was 0.015 at 9.5 GHz.

Through the analysis of the electrical and magnetic losses of the two composite materials in Fig. 6, it could be seen the $Ni/TiO_2/C$ composite contained more carbon material than Ni/TiO_2, resulting in an increase in the electrical loss and a decrease in the magnetic loss of $Ni/TiO_2/C$.

The reflectance (RL) value of a material can directly reflect its electromagnetic wave absorption ability. In order to further analyze the electromagnetic wave absorption performance of the materials, formula (7) was used to calculate the RL value of the materials with different thicknesses. Fig. 7a and b show the relationship between the reflectance of Ni/TiO_2 and $Ni/TiO_2/C$ in the different thickness ranges (1.0–5.5 mm) and frequencies (2–18 GHz). As shown in Fig. 7a, the reflectivity of Ni/TiO_2 decreased with the increase in thickness. At 18 GHz, when the matching thickness was 5.5 mm, the optimal reflectivity was −8.5 dB at 18 GHz. From Fig. 7b, we can see that the reflectivity values of $Ni/TiO_2/C$ were all lower than −10 dB (90% absorption rate) in the range of 2–5.5 mm, and the maximum absorption bandwidth reached 4.4 GHz (6.0–10.4 GHz) at a thickness of 4 mm. When the matching thickness was 3.5 mm, the optimum reflectance of the complex was −40 dB at 10 GHz, and the effective absorption bandwidth could reach 3.74 GHz, and the

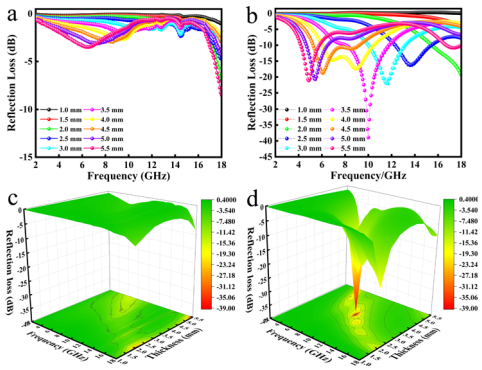

Fig. 7 Relationship between the reflectance (RL) values of (a) Ni/TiO_2; (b) $Ni/TiO_2/C$ and the paraffin complex with frequency and thickness and (c); (d) the corresponding three-dimensional figures.

coverage rate of the band to the X-band (at 8–12 GHz) was 93.5%. These findings indicate that the waveabsorption performance of the $Ni/TiO_2/C$ composite was better than that of Ni/TiO_2, and that $Ni/TiO_2/C$ thus offered a better electromagnetic wave absorption performance.

Fig. 7c and d present three-dimensional maps of Ni/TiO_2 and $Ni/TiO_2/C$ with the reflectivity related to the thickness and frequency. It could be intuitively seen from Fig. 7c that the absorption effect of Ni/TiO_2 was relatively weak, and the reflectivity did not reach −10 dB in the 2–18 GHz range. $Ni/TiO_2/C$ had a remarkable absorption effect on electromagnetic waves (Fig. 7d), and the reflectance values were all less than −10 dB in the thickness range of 2–5.5 mm, and the absorption range was significantly larger than for Ni/TiO_2, which indicated it could effectively absorb electromagnetic waves; and in particular, the X-band absorption effect was better.

Fig. 8 lists some microwave absorption performances for Ni, TiO_2, and carbon material absorbers reported in the literature.[34–43] It can be seen that $Ni/TiO_2/C$ exhibited significant advantages, such as sample loading and ideal RL_{min} values. The advantages of $Ni/TiO_2/C$ could be mainly attributed to the ternary synergistic effect of Ni particles, TiO_2, and carbon materials. Meanwhile, the ideal electromagnetic wave absorption performance of the $Ni/TiO_2/C$ composite material also relies on good impedance matching, and the dielectric loss and magnetic loss.

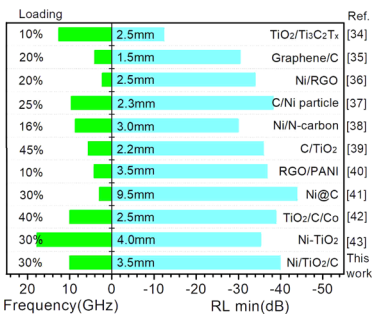

Fig. 8 Summary of the microwave absorption properties of Ni, TiO_2, and carbon material absorbers reported in the literature.

Compared with Ni/TiO_2, and Ni/TiO_2/C composited with carbon materials, the optimal absorption frequency band of Ni/TiO_2/C was shifted to the low frequency band, and the electromagnetic wave absorption rate of Ni/TiO_2/C was significantly improved, while the absorption bandwidth was also significantly wider. In Ni/TiO_2/C, the compositing with a magnetic material (Ni), semiconductor material (TiO_2), and carbon material made its electric loss and magnetic loss cooperate to improve the absorption loss of electromagnetic wave energy. Fig. 9 shows the mechanism of the excellent electromagnetic wave absorption performance of the Ni/TiO_2/C nanocomposite. Based on the above structural characterization and performance analysis, the main absorption loss mechanism is proposed as follows: first, the rod-like structure of Ni/TiO_2/C nanocomposite is beneficial for electromagnetic wave transmission and increasing the losses. The rod structure can reflect and scatter waves multiple times to extend the propagation path of electromagnetic waves, thus enhancing the loss of electromagnetic wave in the refraction process, and can also adjust the effective electromagnetic parameters of the material to improve its impedance matching, so that more electromagnetic waves can enter into the material body, these providing the necessary conditions for the improvement of electromagnetic dissipation. Second, the accumulated charges on the heterojunction interface between the Ni particles and TiO_2 rod surfaces can form a capacitance structure, which will cause enhanced interface polarization and dielectric loss. The two-phase structure appears to be combined, which is favorable for creating abundant local heterogeneous interfaces. It also needs to be mentioned that sufficient lattice defects or distortion derived from the lattice dislocations aided by the fresh interface heterostructure contribute to the dipole orientation polarization.[44] When an EMW is transmitted at the heterogeneous interface between TiO_2/Ni and TiO_2/carbon, it generates polarization and dissipation of the EMW energy.[45] Ni particles can form effective conductive pathways, and the conductivity and impedance matching of the Ni/TiO_2/C nanocomposite are effectively regulated. This further enhances the dissipation of electromagnetic waves by the Ni/TiO_2/C nanocomposite. By increasing the electromagnetic wave absorption value through various forms of interfacial polarization, Ni, TiO_2, and C not only produce enough lattice defects to induce dipole polarization, but also cause uneven spatial charge distribution, thus enhancing the interfacial polarization and improving the electromagnetic wave energy during transmission.[46] Third, natural resonance and eddy currents generated by the magnetoelectricity achieve magnetic losses, while the conductive network formed by the connection of Ni particles maintains the conduction losses.[47,48] Therefore, the magnetic and conduction losses of Ni nanoparticles contribute to the attenuation of electromagnetic waves. In short, each component exerts its own characteristics to improve the electromagnetic wave absorption performance; for instance, the magnetic material (Ni), with high saturation magnetization, high permeability, compatible dielectric loss, and magnetic loss performance in the frequency range of 2–18 GHz; the semiconductor material, TiO_2, which is a common metal oxide material with stable chemical properties. It also has a low synthesis cost, a wide range of raw material sources, and a certain dielectric loss ability; and the carbon materials, which offer the advantages of light weight, strong dielectric loss ability, and an easiness to be compounded with other materials. In particular, the existence of sp^2 orbital hybrid states of carbon atoms endows them with conductivity, exhibiting excellent electromagnetic ohmic and dielectric loss characteristics. Under the induction of external electromagnetic fields, defective relaxation and functional group electron dipole moment polarization relaxation are formed inside the material, thereby the Ni/TiO_2/C material demonstrated increased dielectric loss and an improved EMW absorption performance.

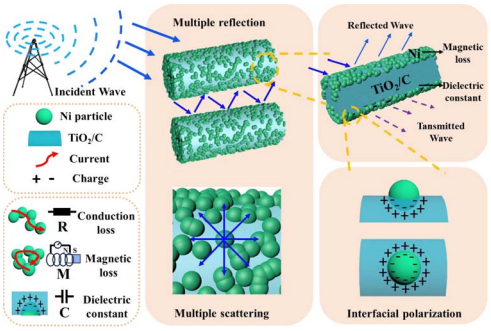

Fig. 9 Schematic illustration of the microwave absorption mechanisms of the Ni/TiO_2/C composite.

4. Conclusions

In this paper, a rod-like Ni/TiO_2/C composite material was prepared, and the morphology, structure, valence state, and magnetism of the material were characterized in detail. The electromagnetic parameters in the range of 2–18 GHz were tested, and the reflectance in the range of 1–5.5 mm was calculated. Compared with Ni/TiO_2, the Ni/TiO_2/C composite material had a better electromagnetic wave absorption ability. The Ni/TiO_2/C material has the characteristics of a wide frequency band, thin, light, and strong, and has broad application prospects.

Conflicts of interest

There are no conflicts to declare.

Acknowledgements

We gratefully acknowledge the support of this research by the Key Research and Development Plan of Heilongjiang province (GZ20210140), the Talent Training Project of the Central Government for the Reform and Development of Local Colleges and Universities (2021GSP13), the Natural Science Foundation of Heilongjiang Province (LH2019B018), the Natural Science Foundation of Heilongjiang Province (LH2021B025), the Fundamental Science Research Funds for of Heilongjiang Provincial Universities (2022GJ08), the National College

Students' Innovative Entrepreneurial Training Plan Program (202211802061, 202211802091).

Notes and references

1 Y. X. Xia, W. Gao and C. Gao, *Adv. Funct. Mater.*, 2022, **32**, 2204591.
2 Z. C. Wu, H. W. Cheng, C. Jin, B. T. Yang, C. Y. Xu, K. Pei, H. B. Zhang, Z. Q. Yang and R. C. Che, *Adv. Mater.*, 2022, **34**, 2107538.
3 X. Liu, M. Li, H. Liu, W. Duan, C. Fasel, Y. Chen, F. Qu, W. Xie, X. Fan, R. Riedel and A. Weidenkaff, *Carbon*, 2022, **188**, 349–359.
4 M. Ying, R. Zhao, X. Hu, Z. Zhang, W. Liu, J. Yu, X. Liu, X. Liu, H. Rong, C. Wu, Y. Li and X. Zhang, *Angew. Chem.*, 2022, **134**, e202201323.
5 S. Rehman, S. Xu, Z. Li, T. Tao, J. Zhang, H. Xia, H. Xu, K. Ma and J. Wang, *Small*, 2023, 2306466.
6 X. Liu, H. Liu, H. Xu, W. Xie, M. Li, J. Liu and G. Liu, *J. Colloid Interface Sci.*, 2022, **606**, 1543.
7 X. Zhang, X. L. Tian, Y. T. Qin, J. Qiao, F. Pan, N. Wu, C. X. Wang, S. Y. Zhao, W. Liu, J. Cui, Z. Qian, M. T. Zhao, J. R. Liu and Z. H. Zeng, *ACS Nano*, 2023, **17**, 12510.
8 H. Wang, Q. Qu, J. Gao and Y. He, *Nanoscale*, 2023, **15**, 8255.
9 X. Liu, H. Xu, G. Liu, W. Duan, Y. Zhang, X. Fan and R. Riedel, *J. Eur. Ceram. Soc.*, 2021, **41**, 480.
10 N. Chen, S. Wei, B. Shi, R. Yan, X. Li and T. Zhan, *J. Ind. Text.*, 2021, **51**, 343.
11 Y. Lu, S. Zhang, M. He, L. Wei, Y. Chen and R. Liu, *Carbon*, 2021, **178**, 413.
12 N. Wu, Q. Hu, R. Wei, X. Mai, P. Duo, Z. Guo and Z. Shi, *Carbon*, 2021, **176**, 88.
13 Y. Chen, L. Cheng, T. Xia, M. Wang, H. Zhou, Q. Yao and Y. Zhai, *Ceram. Int.*, 2022, **48**, 3963.
14 J. Qian, B. Du, M. Cai, C. He, X. Wang, H. Xiong and A. Shui, *Adv. Eng. Mater.*, 2021, **23**, 2100434.
15 Z. Liao, M. Ma, Z. Tong, Y. Bi, K. L. Chung, M. Qiao, Y. Ma, A. Ma, G. Wu, X. Zhong and R. Sun, *Dalton Trans.*, 2021, **50**, 11640.
16 Z. Qin, C. Wang, Y. Ma, J. Wang, B. Zhong, X. Li and P. Zhang, *ACS Appl. Nano Mater.*, 2022, **5**, 7208.
17 B. Li, Z. Zeng, J. Qiao, Y. Yang, D. Xu, H. Tian, W. Liu and J. Liu, *ACS Appl. Nano Mater.*, 2022, **5**, 11617.
18 Y. Liao, G. He and Y. Duan, *Chem. Eng. J.*, 2021, **425**, 130512.
19 H. Lv, C. Wu, J. Tang, H. Du, F. Qin, H. Peng and M. Yan, *Chem. Eng. J.*, 2021, **411**, 128445.
20 D. Zhang, Y. Xiong, J. Cheng, H. Raza, C. Hou, T. Liu, X. Ba, P. Zhang and M. Cao, *Appl. Surf. Sci.*, 2021, **548**, 149158.
21 T. Xia, C. Zhang, A. N. Oyler and X. Chen, *Adv. Mater.*, 2013, **25**, 6905.
22 N. Sun, B. Du, F. Liu, P. Si, M. Zhao, X. Zhang and G. Shi, *J. Alloys Compd.*, 2013, **577**, 533.
23 G. Wan, L. Yu, X. Peng, G. Wang, X. Huang, H. Zhao and Y. Qin, *RSC Adv.*, 2015, **5**, 77443.
24 X. Zhang, W. Zhu, W. Zhang, S. Zheng and S. Qi, *J. Mater. Sci.: Mater. Electron.*, 2018, **29**, 7194.
25 B. Wang, C. Zhang, C. Mu, R. Yang, J. Xiang, J. Song, F. Wen and Z. Liu, *J. Magn. Magn. Mater.*, 2019, **471**, 185.
26 N. Wu, C. Liu, D. Xu, J. Liu, W. Liu, Q. Shao and Z. Guo, *ACS Sustain. Chem. Eng.*, 2018, **6**, 12471.
27 Y. Pan, B. Liu, H. Hu, H. Jiang, F. Wei, M. Zhou, X. Fan, H. Yu, G. Niu and J. Huang, *Vacuum*, 2019, **159**, 1.
28 S. Pigeot-Rémy, D. Gregori, R. Hazime, A. Hérissan, C. Guillard, C. Ferronato, S. Cassaignon, C. Colbeau-Justin and O. Durupthy, *J. Mater. Sci.*, 2019, **54**, 1213.
29 C. Li, Y. Ge, X. Jiang, G. I. N. Waterhouse, Z. Zhang and L. Yu, *Ceram. Int.*, 2018, **44**, 19171.
30 J. Qiao, X. Zhang, C. Liu, L. Lyu, Z. Wang, L. Wu, W. Liu, F. Wang and J. Liu, *Composites, Part B*, 2020, **200**, 108343.
31 L. Lyu, S. Zheng, F. Wang, Y. Liu and J. Liu, *J. Colloid Interface Sci.*, 2021, **602**, 197.
32 B. Zhang, I. Mahariq, N. Tran, M. Z. Mahmoud and M. N. Akhtar, *Ceram. Int.*, 2022, **48**, 446.
33 Y. Qiu, Y. Lin, H. Yang, L. Wang, M. Wang and B. Wen, *Chem. Eng. J.*, 2020, **383**, 123207.
34 B. Zhao, G. Shao, B. Fan, W. Zhao and R. Zhang, *Phys. Chem. Chem. Phys.*, 2015, **17**, 2531.
35 Z. Li, X. Han, Y. Ma, D. Liu, Y. Wang, P. Xu, Y. Du and C. Li, *ACS Sustain. Chem. Eng.*, 2019, **6**, 8904.
36 W. Liu, Q. W. Shao, G. B. Ji, X. H. Liang, Y. Cheng, B. Quan and Y. W. Du, *Chem. Eng. J.*, 2017, **313**, 734.
37 X. Chen, F. Meng, Z. Zhou, X. Tian, L. Shan, S. Zhu, X. Xu, M. Jiang, L. Wang, D. Hui, Y. Wang, J. Lu and J. Gou, *Nanoscale*, 2014, **6**, 8140.
38 M. Han, X. Yin, X. Li, B. Anasori, L. Zhang, L. Cheng and Y. Gogotsi, *ACS Appl. Mater. Interfaces*, 2017, **9**, 20038.
39 C. Li, G. Chen, W. Jiang, X. Jiang, C. Wang and X. Yan, *Appl. Surf. Sci.*, 2021, **556**, 149533.
40 M. Liu, L. Wu, B. Fan, G. Tong, D. B. Chen and W. Wu, *Appl. Surf. Sci.*, 2022, **571**, 151273.
41 Y. Wang, G. Hao, Z. Hui, S. Zhang, X. Ke and H. Yan, *Mater. Today Commun.*, 2022, **30**, 103092.
42 C. Wang, Y. Ding, Y. Yuan, X. He, S. Wu, S. Hu, M. Zou, W. Zhao, L. Yang, A. Cao and Y. Li, *J. Mater. Chem. C*, 2015, **3**, 11893.
43 Y. Tong, M. He, Y. Zhou, S. Nie, X. Zhong, L. Fan and Y. Wang, *ACS Sustain. Chem. Eng.*, 2018, **6**, 8212.
44 W. Deng, T. Li, H. Li, A. Dang, X. Liu, J. Zhai and H. Wu, *Carbon*, 2023, **206**, 192.
45 Y. Qiu, B. Wen, H. Yang, Y. Lin, Y. Cheng and L. Jin, *J. Colloid. Interface Sci.*, 2021, **602**, 242.
46 J. Pan, W. Tu, S. Ma, X. Sun, Q. Zhao, H. Qu and T. Wang, *Dalton Trans.*, 2022, **51**, 9793.
47 B. Bateer, X. M. Zhang, Y. Xie, Y. Y. Dong, X. D. Wang, H. C. Zhang, X. J. Bian and C. G. Tian, *ACS Appl. Eng. Mater.*, 2023, **1**, 1831.
48 L. Wang, M. Huang, X. Qian, L. Liu, W. You, J. Zhang, M. Wang and R. Che, *Small*, 2021, **17**, 2100970.